Ferroelectricity, triple-well potential, and negative piezoelectricity in the antiperovskite γ-Ag_3SI

Xiaonan Ma,[1,2,*] Chang Liu,[1,2,*] Giuliana Materzanini,[2] Gian-Marco Rignanese,[2] and Wei Ren[1,†]

[1]*Physics Department, Material Genome Institute, Shanghai Engineering Research Center for Integrated Circuits and Advance Display Materials, Institute for Quantum Science and Technology, International Center for Quantum and Molecular Structures, Shanghai University, Shanghai 200444, China*

[2]*Institute of Condensed Matter and Nanosciences, Université catholique de Louvain, B-1348 Louvain-la-Neuve, Belgium*

(Received 19 April 2024; revised 7 August 2024; accepted 12 September 2024; published 12 November 2024)

Various perovskites, such as $BaTiO_3$, exhibit ferroelectric distortion driven by long-range Coulomb interactions and *d-p* orbital hybridization. Antiperovskites, with a structure resembling perovskites but with inverted cations and anions, display significantly distinct physical properties in terms of ferroelectricity and piezoelectricity despite their structural similarities. However, the literature on these materials is scarce. Among them, Ag_3SI, a three-dimensional antiperovskite superionic conductor, demonstrates exceptional ionic conduction in nonpolar phases (α and β) but shows reduced conductivity in the polar phase (γ). Our study uncovers the unconventional mechanism of ferroelectricity in Ag_3SI: an anomalous *s-d* orbital self-mixing in the polar γ phase, originating from Ag^+ short-range interactions. Additionally, this antiperovskite exhibits two rare phenomena in three-dimensional solid state: a triple-well potential and negative longitudinal piezoelectric effect. Our investigation of Ag_3SI, establishes a theoretical framework to grasp ferroelectricity and negative piezoelectricity in antiperovskites, enriching our understanding of these captivating materials.

DOI: 10.1103/PhysRevB.110.184109

I. INTRODUCTION

Ferroelectricity was first observed in Rochelle salt over a century ago [1,2], but its applications only became prominent after its discovery in perovskite oxides in the 1950s [3]. Nowadays, various industrial exploitations, including sensors, actuators, and memories, rely on electric-field switchable ferroelectric polarization [4]. Regarding the fundamental understanding of this phenomenon, Cochran initially proposed that ferroelectric phase transitions stem from "soft" (i.e., unstable) vibrational modes of the crystal [5]. Later, Bersuker suggested the second-order Jahn-Teller effect as the microscopic origin of ferroelectricity in cubic perovskites [6]. The advent of density-functional theory (DFT) enabled deeper insights into lattice dynamics of ferroelectric perovskites [7]. Cohen demonstrated the differences in ferroelectric behavior between $BaTiO_3$ and $PbTiO_3$ perovskites, highlighting the delicate balance between short-range repulsion promoting the nonpolar cubic structure and long-range Coulomb interactions favoring the ferroelectric state. This equilibrium is underpinned by the crucial hybridization between Ti $3d^0$ and O $2p$ states, essential for the manifestation of ferroelectricity properties [8]. Expanding on Cochran's model and Cohen's theory, Ghosez *et al.* calculated the unusually large Born effective charges due to significant Ti $3d^0$ and O $2p$ states' covalent bonding in ABO_3 perovskites [9], and quantified the forces balance leading to unstable phonons in cubic phase of $BaTiO_3$ [10]. These previous reports support our current understanding of ferroelectricity in perovskites.

A_3BX antiperovskite compounds form a family of interesting materials that possess a structure similar to perovskites, but with inverted cations and anions [11,12]. Their diverse physical properties have drawn great attention, ranging from superionic conductivity [13–15] and the strong spin-lattice coupling [16–18] to the topological electronic behavior [19,20]. However, discussions on ferroelectricity and phase transitions in antiperovskites are scarce. Ag_3SI synthesized by Reuter and Hardel exhibits a high-temperature α phase and a room-temperature β phase with high ionic conductivity [21,22]. Hoshino *et al.* discovered a third ordered phase, the γ phase below 157 K, indicating an order-disorder (γ-β) phase transition related to Ag^+ distribution [23,24]. This γ phase exhibits pyroelectricity [23–25], yet establishing ferroelectric behavior through hysteresis-loop measurement proved challenging due to Ag^+ ions' mobility [25]. This intriguing behavior prompts investigation into ferroelectricity in Ag_3SI, and comparison with the traditional $BaTiO_3$.

In this work, we utilize DFT calculations to investigate the β- and γ phases of Ag_3SI. The computational methodologies are described in the Supplemental Material [26] (see also Refs. [27–44] therein). Our analysis reveals that the ferroelectric distortion in Ag_3SI is driven by an unusual Ag^+ *s-d* orbital self-mixing mechanism. While a double-well potential is the most common trait of ferroelectrics, our results from climbing image nudged elastic band (CI-NEB) demonstrate that Ag_3SI exhibits both double and triple-well potentials. Furthermore, under hydrostatic pressures ranging from 0 to 150 GPa, we observe that the ferroelectric behavior of Ag_3SI, more precisely its structure distortion, originates from short-range interactions rather than long-range Coulomb ones, leading to a negative piezoelectric effect and a gradual increase of the

*These authors contributed equally to this work.
†Contact author: renwei@shu.edu.cn

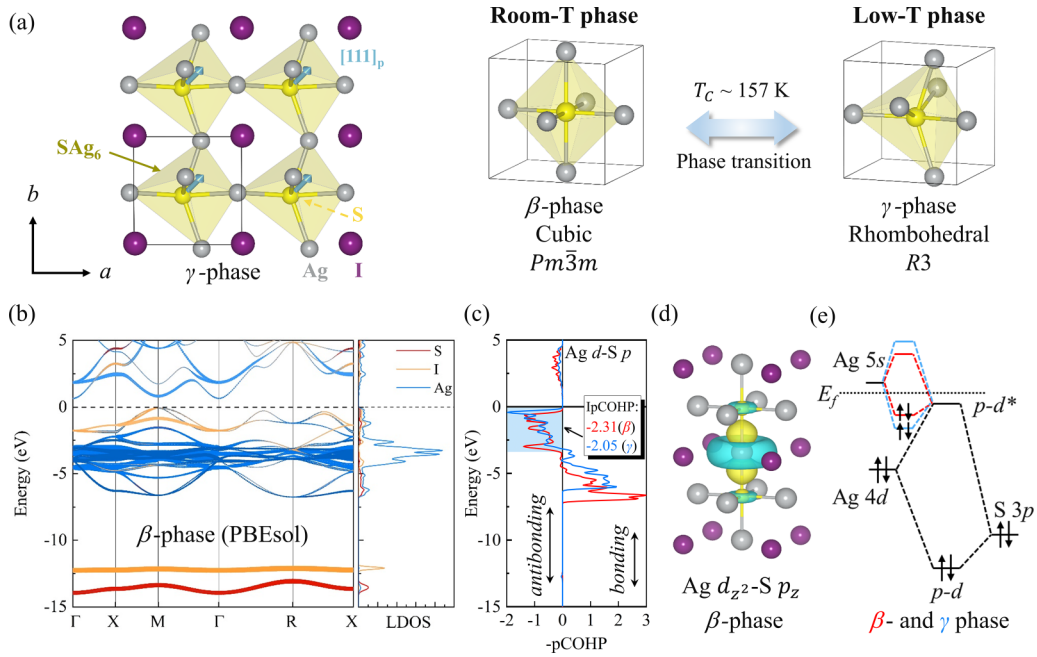

FIG. 1. Structural comparison of β ($Pm\bar{3}m$) and γ ($R3$) phases of Ag_3SI. (a) Top view of γ-Ag_3SI with a polarization along the [111] direction in each unit cell, illustrating the phase transition between the β and γ phases. (b) Band structure and local density of states of β-Ag_3SI. (c) pCOHP analysis of the S^{2-} with three-neighbor Ag^+ interaction in β (red) and γ (blue) phases. Positive and negative values of pCOHPs indicate bonding (d-p) and antibonding states (d-p*), respectively. Integrated pCOHP (IpCOHP) values for antibonding states of the β and γ phases are reported. (d) Valence-band MLWFs for the β phase showing the occupied antibonding states (the isosurfaces are illustrated for 1.08×10^{-8} a.u., with the positive values in yellow and the negative values in blue). (e) Schematic energy-level diagram of Ag–S orbitals of β (red) and γ (blue) Ag_3SI.

electric polarization. These findings shed light on the ferroelectric properties of antiperovskites, distinguishing them from conventional ferroelectric perovskites and advancing our understanding of this unique compound.

II. RESULTS AND DISCUSSION

Ag_3SI is a three-dimensional antiperovskite superionic conductor composed of silver (Ag^+) cations, sulfur (S^{2-}), and iodine (I^-) anions. Powder neutron diffraction has revealed three stable phases: the α phase at high temperature ($T > 519$ K, $Im\bar{3}m$), the β phase at room temperature ($157\ \text{K} < T < 519$ K, $Pm\bar{3}m$), and the γ phase at low temperature ($T < 157$ K, $R3$). Impedance spectroscopy measurements have confirmed the superionic nature of the α and β phases [45]. Furthermore, the γ-β phase transition at 157 K was found to be of both structural and order-disorder nature [23,24]. The γ phase exhibits long-range ordering of the cations on a subset of displaced octahedral positions, along with a slight displacement of the S^{2-} anions along the [111] direction [45]. While the γ phase is suggested to be ferroelectric, its high ionic conductivity poses challenges for reliable dielectric property measurements [25]. In Fig. 1(a), we illustrate, for simplicity, the ordered γ phase in a cubic supercell, showing the S^{2-} ions at the center of the Ag^+ octahedra, and the I^- ions at the cell corners [23–25,46,47]. The calculated lattice constants for the β- and γ phases are 4.86 and 4.80 Å, respectively. Using the Berry phase approach, we compute a polarization of 14.57 μC/cm^2 along the [111] direction in the γ phase, attributed to the displacement of Ag^+ cations with respect to the octahedral positions, and to the slight displacement of S^{2-} anions [45].

In this study, we present electronic structure calculations for the β and γ phases of Ag_3SI, with corresponding band-gap values of 0.72 and 0.56 eV, respectively [see Fig. 1(b) and Table S1]. We further analyze the integrated crystal-orbital bond index (ICOBI) to assess bond covalency, which ranges from 0 (indicating 100% ionic character) to a maximum of 1 (representing 100% covalent character) [48,49]. The calculated ICOBI values for the Ag–S bond are 0.25 and 0.22 for the β and γ phases, respectively. These low values indicate a significant ionic contribution to the Ag–S bond in Ag_3SI, although not as pronounced as in a typical ionic bond, such as Na–Cl in the rocksalt NaCl (with an ICOBI value of 0.09) [48]. Notably, these ICOBI values are much smaller than those of the covalent Ti–O bond in $BaTiO_3$, for which values of 0.64 and 0.91 were reported in the paraelectric and ferroelectric phases, respectively [48]. The more ionic character of the Ag–S bond in Ag_3SI compared to the Ti−O bond is supported by the Born effective charges and the Bader analysis (see Table S2). The Born effective charges for Ag–S are closer to the nominal charges (Ag: 1.30e, S: −1.52e), whereas for Ti–O, they are anomalously high (O: −5.87e, Ti: 7.41e), indicating a higher degree of covalency. Furthermore, the Bader charges reveal a relatively weak covalent character for the Ag–S bond (Ag: 0.34e, S: −0.40e), compared to the Ti–O bond (O: −1.20e, Ti: 2.05e), as shown in Table S2.

Here, we investigate the bonding mechanisms in the β and γ phases of Ag_3SI using the projector crystal-orbital Hamilton population (pCOHP) [49], partial charge density,

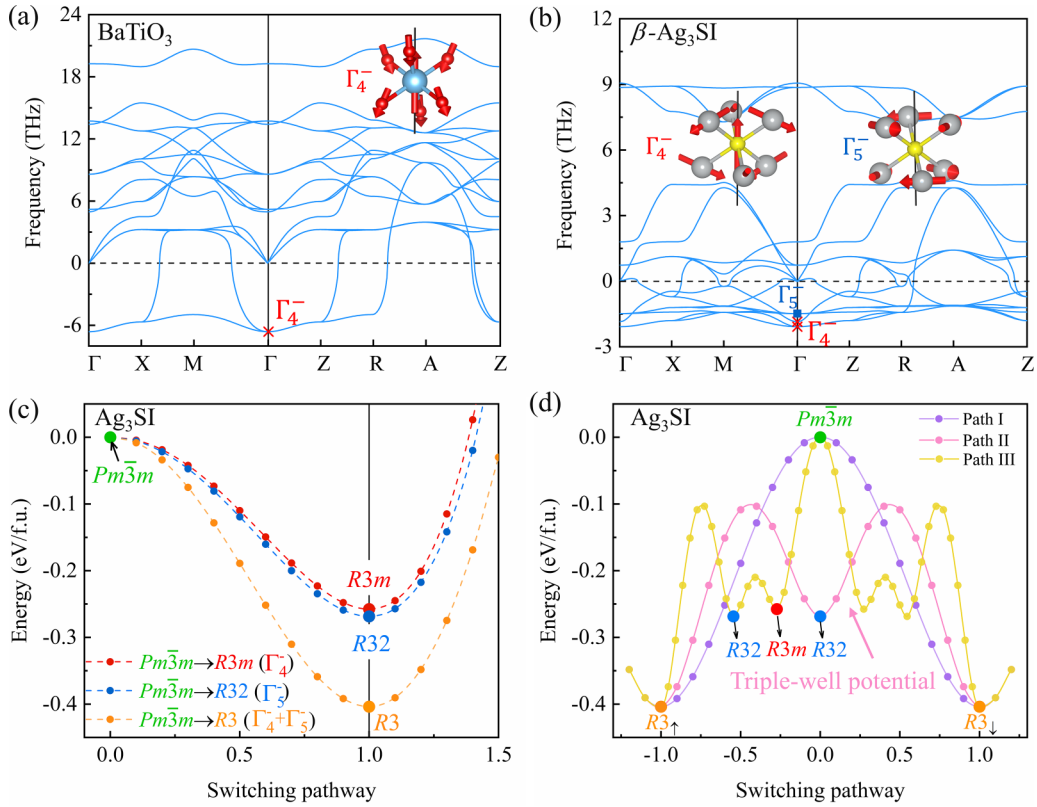

FIG. 2. Phonon spectra and energy-potential profiles: (a), (b) Phonon spectra of the $Pm\bar{3}m$ phase of $BaTiO_3$ and Ag_3SI, highlighting imaginary frequency modes at the Γ point. The red crosses (×) represent Γ_4^-, and the blue solid rectangles (■) represent Γ_5^-. (c) Energy profiles along the switching pathways following two imaginary modes (Γ_4^- and Γ_5^-) at the Γ point. The energy of the $Pm\bar{3}m$ phase is reported at $x = 0$, while the energies of the $R3m$, $R32$, and $R3$ phases, which were obtained by freezing the Γ_4^- mode, the Γ_5^- mode, and the combination of both modes, are indicated at $x = 1$, with the switching pathways shown in red, blue, and orange, respectively. (d) Energy profiles along three switching pathways calculated by NEB method: Path I (purple) from $R3$ ($|x| = 1$) to $Pm\bar{3}m$ ($x = 0$); Path II (pink) from $R3$ ($|x| = 1$) to $R32$ ($x = 0$); Path III (yellow) corresponds to $R3$ ($|x| = 1$) → $R32$ → $R3m$ → $Pm\bar{3}m$ ($x = 0$). $R3_\uparrow$ and $R3_\downarrow$ denote two $R3$ states with opposite polarizations.

and maximally localized Wannier functions (MLWFs) [50]. In Fig. 1(c), the bonding states below the Fermi level at −5 eV involve closed-shell Ag e_g (d_{z^2} and $d_{x^2-y^2}$) and S 3p orbitals, with bands primarily originating from the Ag 4d states, including nonbonding states. The antibonding states occupy the top of the valence band (Fig. S1). The Ag^+ d-p hybridization, previously studied in Ag^+ and Cu^+ superionic conductors, is correlated with the activation energy for Ag^+/Cu^+ conductivity [51–54]. In Fig. 1(d), the MLWF illustrates Ag d_{z^2} and S p_z orbitals forming a σ^* antibonding state, similar to the bonding states in the conduction band of perovskite oxides [55]. The absolute values of the integrated pCOHP (IpCOHP) for the d-p^* antibonding states in β- and γ-Ag_3SI (2.31 and 2.05, respectively) indicate a more significant d-p^* antibonding interaction in the nonpolar phase. The partial density of states (PDOS) plots (Fig. S3) display significant overlap between 5s and d_{z^2} states at ∼7 eV below the Fermi energy for both phases, with more effective s-d orbital mixing in the γ phase, as suggested by larger integrated PDOS for the Ag 5s states in the valence bands for γ- than for β-Ag_3SI (Table S3). This enhanced s-d mixing in the γ phase is schematically depicted in Fig. 1(e), representing the second-order Jahn-Teller coupling that stabilizes the polar phase against the nonpolar one. Specifically, the initial step involves the admixture of occupied d-p^* antibonding states, followed by their mixing with unoccupied Ag 5s orbitals. Similar results were reported for PbO and SnO in Refs. [56,57], where hybridization between cation states and cation-anion antibonding states stabilized occupied electronic states only in the presence of crystal distortion, due to symmetry considerations [56]. This finding aligns with the experimental observation of d-orbital holes in Cu_2O [58] and theoretical works showing that the metal s-d orbital mixing is a predominant factor driving the instabilities in CuCl and CuBr [59–62]. The orbital mixing lifts the degeneracy of antibonding Ag e_g^* states (Fig. S4). Additionally, replacing sulfur with selenium and oxygen lowers the anion p level, weakening d-p^* antibonding interactions and reducing the frequency of the imaginary polar mode in the $Pm\bar{3}m$ phase (Fig. S5).

III. PHONON INSTABILITY AND TRIPLE-WELL POTENTIAL

In Figs. 2(a) and 2(b), we present the phonon spectra for $BaTiO_3$ and Ag_3SI, calculated from first principles, with LO-TO splitting considered. We focus on the soft modes at the Γ point, particularly the polar mode Γ_4^- common to both materials. In this mode, Ag^+ (O^{2-}) and S^{2-} (Ti^{4+}) ions move

TABLE I. Squared frequency ω^2 of the Γ_4^- transverse optical mode for $BaTiO_3$ and Ag_3SI at zero pressure. The squared frequency is decomposed into the short-range (ω^2_{SR}) and long-range (ω^2_{LR}) contributions.

	$BaTiO_3$ (10^5 cm^{-2})	β-Ag_3SI (10^5 cm^{-2})
ω^2	0.52476	0.54560
ω^2_{SR}	6.27702	−0.83982
ω^2_{LR}	−6.80178	0.29422

relative to each other along the threefold rotation axis, resulting in a polarization along the pseudocubic [111] direction. Additionally, Ag_3SI exhibits a nonpolar Γ_5^- mode, involving the clockwise rotation of the upper Ag^+ and counterclockwise rotation of the lower Ag^+ along the same axis [Fig. 2(b)]. Freezing only the Γ_4^- mode in $BaTiO_3$ results in the $R3m$ ground-state ferroelectric structure [63,64], whereas freezing either the Γ_4^- or Γ_5^- mode in Ag_3SI leads to metastable structures with space groups $R3m$ or $R32$, respectively [Fig. 2(c)]. Simultaneously freezing both modes results in the lowest-energy structure, with space group $R3$, corresponding to the polar γ-Ag_3SI, as validated by neutron-diffraction refinement experiments [45].

We then investigate the ferroelectric polarization switching of γ-Ag_3SI using the CI-NEB method [Fig. 2(d)] [65]. Three possible paths for polarization switching are considered, involving the metastable $R3m$, metastable $R32$, and $Pm\bar{3}m$ (β-Ag_3SI) structures, between two $R3$ (γ-Ag_3SI) structures with opposite polarization. Note that the applied electric field only affects the Γ_4^- polar distortion mode, which relates to the $R3m$ structure. The lowest-energy path is the one going through the nonpolar $R32$ (path II). It has an energy barrier of approximately 0.3 eV/f.u. (per formula unit) and a triple-well energy profile, with the $R32$ structure as a local minimum. Such a triple-well potential has also been predicted in ferroelectric potassium nitrate, KNO_3 [66] and $Sn_2S_2P_6$ [67], but it is rare in ferroelectric perovskites and antiperovskite systems, and ferroelectrics in general [68–70]. The path involving the $Pm\bar{3}m$ structure (path I) displays a typical double-well energy profile with a higher barrier (0.4 eV/f.u.). Path III, involving the polar metastable $R3m$ structure, exhibits a more complex energy profile, with again a 0.4 eV/f.u. barrier, where the $Pm\bar{3}m$ structure serves as the transition state, and both $R3m$ and $R32$ structures are local minima.

We now analyze the contributions of long-range and short-range interactions to the unstable modes of cubic $BaTiO_3$ and β-Ag_3SI. It is well established that in oxide ferroelectric perovskites like $BaTiO_3$, short-range repulsion favors the high-symmetry (cubic) paraelectric state, while long-range (dipole-dipole) electrostatics favors the low-symmetry ferroelectric state [8,10]. In Table I, following the methodology of Ref. [71], we decompose the unstable Γ_4^- mode of cubic ($Pm\bar{3}m$) $BaTiO_3$ into short-range (ω^2_{SR}) and long-range (ω^2_{LR}) contributions. The latter originates from dipole-dipole interactions responsible for the structural distortion in the paraelectric phase. We observe that $\omega^2_{SR} > 0$ and $\omega^2_{LR} < 0$, with LR forces dominating to induce a net phonon instability and ferroelectric polarization in $BaTiO_3$ [72]. As shown in Table I, the Γ_4^- mode of β-Ag_3SI exhibits instability, but with opposite signs for SR and LR contributions compared to $BaTiO_3$: the SR contribution is negative, and the LR is positive, driving the instability of the polar phase through SR interactions. This could stem from the intrinsic disorder of the three Ag^+ ions per unit cell in β phase, potentially leading to close proximity and distortions in Ag_3SI. Notably, the negative onsite force constants of Ag ($x = y$) mainly arise from its SR part (−0.00930 hartree/bohr^2, Table S4). In contrast, cooperative LR interactions between Ti and O induce structural distortions in $BaTiO_3$ [7,71]. The Γ_5^- mode, responsible for polar distortion, also exhibits negative contributions from both ω^2_{SR} and ω^2_{LR} (Fig. S7). Overall, the origin of ferroelectricity in β-Ag_3SI differs from cubic $BaTiO_3$: in β-Ag_3SI SR forces favor the distorted polar structure, while in cubic $BaTiO_3$, LR interactions drive ferroelectric distortion. This distinction can be attributed to the strong covalent bonding in $BaTiO_3$, resulting in large Born effective charges [9], significant LO-TO splitting [73], and strong LR Coulomb interaction [74]. Conversely, for β-Ag_3SI, indicators such as ICOBI, the Born effective charges, and Bader analysis suggest a more ionic bond character.

IV. PHONON MODES UNDER PRESSURE AND NEGATIVE PIEZOELECTRICITY

We now discuss phonon instability under pressure, depicted in Figs. 3(a) and 3(b) for cubic $BaTiO_3$ and β-Ag_3SI, respectively. In cubic $BaTiO_3$, the overall phonon instability decreases under pressure, eventually disappearing at ∼20 GPa [red curve in Fig. 3(a)]. In contrast, for β-Ag_3SI, the instability continuously increases under pressure [red curve in Fig. 3(b)]. This anomaly can be understood by analyzing the absolute IpCOHP values for Ag–S d-p* antibonding and Ag–S s-p bonding states under pressure in γ-Ag_3SI, as shown in Fig. S11. Both populations increase under pressure, indicating that pressure enhances the s-d mixing, which in turn stabilizes the γ phase. Therefore, we conclude that the γ phase is favored by pressure, which is consistent with the continuous increase in polar instability of β-Ag_3SI under pressure [Fig. 3(b)].

In Figs. 3(a) and 3(b), we present LR and SR contributions to phonon instability. For cubic $BaTiO_3$, LR interactions drive instability at low pressure. As the pressure increases, the LR contribution rises while the SR contribution decreases, with their signs changing around 60 GPa. This delicate balance suppresses the instability of the Γ_4^- mode at ∼20 GPa, consistent with Ref. [71] (and Ref. [10]). At 140 GPa, the squared frequency of the Γ_4^- mode turns negative again, also in agreement with Ref. [71]. Kornev and Bellaiche attribute the reappearance of ferroelectricity under pressure to increased hybridization between Ti e_g and O 2s orbitals [72]. For β-Ag_3SI, the instability of the Γ_4^- mode increases with pressure due to a significant decrease in ω^2_{SR} while ω^2_{LR} weakly increases, both maintaining their respective signs. This indicates an enhanced role of SR forces in driving polar instability in β-Ag_3SI under pressure. Similar behavior is observed in materials such as hyperferroelectricity anti–Ruddlesden-Popper ferroelectrics [75], $LiNbO_3$-type systems, and hexagonal-ABC systems [76–78]. For instance, in the

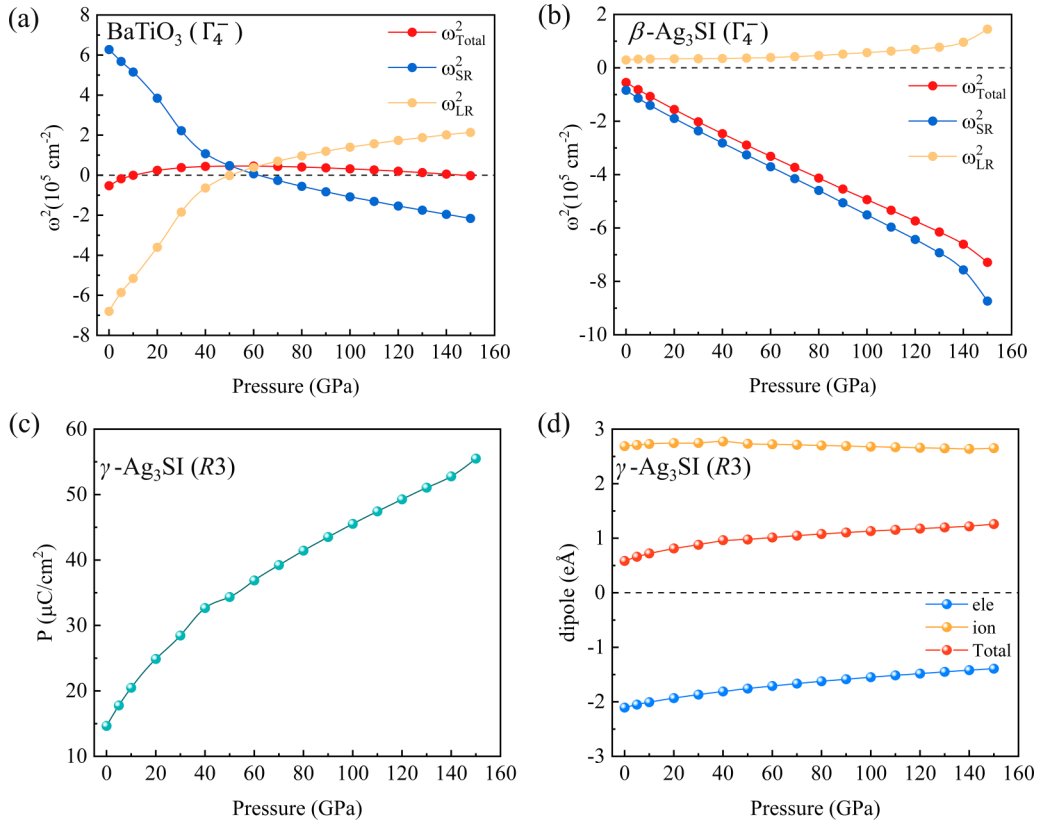

FIG. 3. Squared frequency of the Γ_4^- transverse optical mode for (a) $BaTiO_3$ and (b) Ag_3SI. The squared frequencies (total in red) are decomposed into the contributions due to the short-range (SR in blue) and long-range (LR in orange) interactions. (c) Evolution of the polarization of $R3$-Ag_3SI under pressure. (d) Total dipole moment (red line) under pressure, and its electronic (blue line) and ionic (yellow line) contributions.

latter, short-range pair interactions among local dipole modes not only drive ferroelectric long-range ordering of local polar distortion but also stabilize $LiOsO_3$ [78].

Direct piezoelectricity is a reversible phenomenon where mechanical stress induces electric dipoles in a material, changing its polarization. In Eq. (1), ΔP represents the induced polarization, σ is the applied stress in Voigt notation, and the piezoelectric strain d is a third-rank tensor [79]:

$$\Delta P_i = d_{ij}\sigma_j. \tag{1}$$

From the piezoelectric strain tensor d, we define the piezoelectric stress tensor e through the elastic stiffness tensor C [80]:

$$e_{ik} = C_{kj}\, d_{ij}. \tag{2}$$

So, Eq. (1) can also be written in terms of the applied strain η:

$$\Delta P_i = e_{ij}\eta_j. \tag{3}$$

All ferroelectric materials are also piezoelectrics, with piezoelectricity being discovered in $BaTiO_3$ long before its ferroelectric behavior [81]. In traditional ferroelectrics, mechanical expansion enhances the polarization, while compression suppresses it. Typically, the piezoelectric strain coefficient d_{ij} is positive, indicating that tensile strain η_j along the $P_i > 0$ axis increases the polarization (positive piezoelectric effect). In Fig. 3(c), we show the polarization of γ-Ag_3SI along the polar axis [111] under hydrostatic pressure. Unlike most ferroelectrics, γ-Ag_3SI demonstrates increased polarization under hydrostatic pressure, known as the negative longitudinal piezoelectric effect (NLPE) [82]. Figure 3(d) illustrates that this polarization increase is not solely due to volume reduction under hydrostatic pressure but also involves the enhancement of the dipole moment within the unit cell. We observe a significant increase in the electronic contributions to the dipole moment, indicating that a substantial part of NLPE comes from the electronic contribution. We further perform density-functional perturbation theory calculations of piezoelectric tensor [Eqs. (1) and (4)], considering the polar axis along z. The computed piezoelectric coefficients e_{33} and d_{33} are -0.29 C/m^2 and -2.08 pm/V, respectively (Table S5), confirming the NLPE reported in Figs. 3(c) and 3(d). The piezoelectric coefficients can be decomposed into a clamped-ion term $\bar{e}_{33}$ and an internal-strain term e'_{33} [82–84], with the former reflecting purely electronic effects and the latter representing ionic contributions, proportional to Born effective charges [85]:

$$e_{ij} = \bar{e}_{ij} + e'_{ij} = \bar{e}_{ij} + \Omega_0^{-1} Z^*_{ij} \Phi^{-1}_{jk} \Lambda_{kl}. \tag{4}$$

Here, the rightmost term of this equation shows the ionic contributions to piezoelectric tensor. Ω_0 is the unit-cell volume, Z^*_{ij} is the Born effective charge, Φ^{-1}_{jk} represents the force constants, and Λ_{kl} is the force-response internal strain tensor (see Supplemental Material [26]).

NLPE has been observed in various van der Waals (vdW) layered ferroelectrics [86–88], quasi-2D ferroelectrics, and strong ionic systems [82,86,89]. In layered ferroelectrics like $CuInP_2S_6$, NLPE may can be explained as follows. On the one hand, the positive contribution e'_{33} becomes approximately zero due to weak vdW interactions between molecular layers [86]. On the other hand, $\bar{e}_{33}$ typically shows negative values due to the so-called "lag of the Wannier center" effect, whereby Wannier centers cannot follow a homogeneous strain of atomic fractional coordinates during volume expansion [86]. However, there are special cases, such as in HfO_2 quasi-2D ferroelectrics, where $\bar{e}_{33} > 0$, indicating a positive correlation of the Wannier center with applied strain. NLPE in HfO_2 can be attributed to a negative e'_{33}, due to short Hf–O bonds maintaining equilibrium distance under strain, resulting in an abnormal response of the internal-strain part [82]. This contrasts with ferroelectric perovskites with strong covalency, where e'_{33} is usually positive and larger than $\bar{e}_{33}$, leading to a positive piezoelectric effect [82]. For γ-Ag_3SI, we find that $\bar{e}_{33}$ is -0.14 C/m^2, a negative value consistent with most piezoelectrics and Ref. [86]. However, the contribution of e'_{33} is also negative (-0.15 C/m^2), similar to the negative internal strain observed in HfO_2, as indicated by Λ_{33} (see Supplemental Material [26]). Additionally, both small Born effective charges and ionic characteristics of the bond also play a crucial role in NLPE. Similar to NaZnSb hexagonal-*ABC* ferroelectrics with strong ionic bonds and Bi elemental ferroelectrics, their NLPEs stems from a common negative contribution from $\bar{e}$ and e' [82,90]. Further details of the piezoelectric coefficients can be found in Tables S5 and S6.

V. CONCLUSIONS

In this study, we have conducted a comprehensive investigation of the electronic structure, chemical bonds, phonon instability, and pressure-dependent polarization of the γ and β phases of Ag_3SI antiperovskite using first-principles calculations, with a specific focus on the ferroelectric and piezoelectric properties of γ-Ag_3SI. Our findings highlight a high degree of ionicity in the bonding of Ag_3SI, with the polar phase stabilized by an unusual *s-d* hybridization among Ag^+ cations, contrasting with the typical *d-p* hybridization in ferroelectric perovskites. The analysis of the phonon instability modes in β-Ag_3SI suggests that short-range forces, likely arising from repulsion among Ag^+ ions on adjacent sites, drive the polar distortion, diverging from the long-range interactions prevalent in traditional perovskite ferroelectrics. Moreover, our study identifies a low-barrier path for polarization switching, involving a metastable nonpolar phase (*R*32) as an alternative to β-Ag_3SI, characterized by a triple-well energy profile. Notably, we observe a continuous increase in polar instability with pressure, leading to a pronounced negative longitudinal piezoelectric effect. This effect is attributed to the ionic nature of the bond and to the small Born effective charges, resulting in a negative internal-strain piezoelectric coefficient reminescent of some strong ionic systems. The intriguing electronic structure and phonon-related features uncovered in Ag_3SI underscore its potential as a valuable case study for antiperovskites and offer promising directions for the future design of a remarkable class of ferroelectrics.

ACKNOWLEDGMENTS

This work was supported by National Natural Science Foundation of China (Grants No. 12074241, No. 12311530675, and No. 52130204), Science and Technology Commission of Shanghai Municipality (Grants No. 22XD1400900, No. 20501130600, No. 21JC1402700, No. 21JC1402600, and No. 22YF1413300), Key Research Project of Zhejiang Laboratory (Grant No. 2021PE0AC02), Shanghai Technical Service Center of Science and Engineering Computing, Shanghai University, Shanghai Technical Service Center of Science and Engineering Computing, Shanghai University, and China Scholarship Council. G.M.R. acknowledges useful discussions with B. Xu.

[1] K. M. Rabe, M. Dawber, C. Lichtensteiger, and J.-M. Triscone, *Physics of Ferroelectrics: A Modern Perspective*, Modern Physics of Ferroelectrics: Essential Background (Springer Science+Business Media, Berlin, 2007).

[2] J. Valasek, Piezo-electric and allied phenomena in Rochelle salt, Phys. Rev. **17**, 475 (1921).

[3] J. C. Slater, The Lorentz correction in barium titanate, Phys. Rev. **78**, 748 (1950).

[4] J. F. Scott, Applications of modern ferroelectrics, Science **315**, 954 (2007).

[5] W. Cochran, Crystal stability and the theory of ferroelectricity, Phys. Rev. Lett. **3**, 412 (1959).

[6] I. B. Bersuker, On the origin of ferroelectricity in perovskite-type crystals, Phys. Lett. **20**, 589 (1966).

[7] P. Ghosez, E. Cockayne, U. V. Waghmare, and K. M. Rabe, Lattice dynamics of $BaTiO_3$, $PbTiO_3$, and $PbZrO_3$: A comparative first-principles study, Phys. Rev. B **60**, 836 (1999).

[8] R. E. Cohen, Origin of ferroelectricity in perovskite oxides, Nature (London) **358**, 136 (1992).

[9] P. Ghosez, J.-P. Michenaud, and X. Gonze, Dynamical atomic charges: The case of ABO_3 compounds, Phys. Rev. B **58**, 6224 (1998).

[10] P. Ghosez, X. Gonze, and J. P. Michenaud, Coulomb interaction and ferroelectric instability of $BaTiO_3$, Europhys. Lett. **33**, 713 (1996).

[11] S. V. Krivovichev, Minerals with antiperovskite structure: A review, Z. Kristallogr. **223**, 109 (2008).

[12] Y. Wang, H. Zhang, J. Zhu, X. Lü, S. Li, R. Zou, and Y. Zhao, Antiperovskites with exceptional functionalities, Adv. Mater. **32**, 1905007 (2019).

[13] Y. Zhao and L. L. Daemen, Superionic conductivity in lithium-rich anti-perovskites, J. Am. Chem. Soc. **134**, 15042 (2012).

[14] A. Emly, E. Kioupakis, and A. Van der Ven, Phase stability and transport mechanisms in antiperovskite Li_3OCl and Li_3OBr superionic conductors, Chem. Mater. **25**, 4663 (2013).

[15] Y. Wang, T. Wen, C. Park, C. Kenney-Benson, M. Pravica, W. Yang, and Y. Zhao, Robust high pressure stability and negative thermal expansion in sodium-rich antiperovskites Na_3OBr and Na_4OI_2, J. Appl. Phys. **119**, 025901 (2016).

[16] C. X. Quintela, K. Song, D. F. Shao, L. Xie, T. Nan, T. R. Paudel, N. Campbell, X. Pan, T. Tybell, M. S. Rzchowski *et al.*, Epitaxial antiperovskite/perovskite heterostructures for materials design, Sci. Adv. **6**, eaba4017 (2020).

[17] D. Torres-Amaris, A. Bautista-Hernandez, R. González-Hernández, A. H. Romero, and A. C. Garcia-Castro, Anomalous Hall conductivity control in Mn_3NiN antiperovskite by epitaxial strain along the kagome plane, Phys. Rev. B **106**, 195113 (2022).

[18] K. Shi, Y. Sun, C. V. Colin, L. Wang, J. Yan, S. Deng, H. Lu, W. Zhao, Y. Kazunari, P. Bordet, and C. Wang, Investigation of the spin-lattice coupling in $Mn_3Ga_{1-x}Sn_xN$ antiperovskites, Phys. Rev. B **97**, 054110 (2018).

[19] Y. Sun, X. Q. Chen, S. Yunoki, D. Li, and Y. Li, New family of three-dimensional topological insulators with antiperovskite structure, Phys. Rev. Lett. **105**, 216406 (2010).

[20] R. Yu, H. Weng, Z. Fang, X. Dai, and X. Hu, Topological node-line semimetal and Dirac semimetal state in antiperovskite Cu_3PdN, Phys. Rev. Lett. **115**, 036807 (2015).

[21] B. Reuter and K. Hardel, Silbersulfidbromid und silbersulfidjodid, Angew. Chem. **72**, 138 (1960).

[22] L. Yin, M. Murphy, K. Kim, L. Hu, J. Cabana, D. J. Siegel, and S. H. Lapidus, Synthesis of antiperovskite solid electrolytes: Comparing Li_3SI, Na_3SI, and Ag_3SI, Inorg. Chem. **59**, 11244 (2020).

[23] S. Hoshino, T. Sakuma, and Y. Fujii, A structural phase transition in superionic conductor Ag_3SI, J. Phys. Soc. Jpn. **47**, 1252 (1979).

[24] S. Hoshino, T. Sakuma, and Y. Fujii, The existence of the order phase in superionic conductor Ag_3SI, J. Phys. Soc. Jpn. **45**, 705 (1978).

[25] S. Hoshino, H. Fujishita, M. Takashige, and T. Sakuma, Phase transition of Ag_3SX (X = I, Br), Solid State Ionics **3**, 35 (1981).

[26] See Supplemental Material at http://link.aps.org/supplemental/10.1103/PhysRevB.110.184109 for the details of calculation methods; the structures and electronic structures of Ag_3SI; the pCOHP analysis; the symmetry mode analysis; the interatomic force constants; and the analysis of the negative longitudinal piezoelectric effect. Supplemental Material also contains Refs. [27–44].

[27] A. Jain, S. P. Ong, G. Hautier, W. Chen, W. D. Richards, S. Dacek, S. Cholia, D. Gunter, D. Skinner, G. Ceder, and K. A. Persson, Commentary: The Materials Project: A materials genome approach to accelerating materials innovation, APL Mater. **1**, 011002 (2013).

[28] X. Gonze, J. M. Beuken, R. Caracas, F. Detraux, M. Fuchs, G. M. Rignanese, L. Sindic, M. Verstraete, G. Zerah, F. J. Jollet *et al.*, First-principles computation of material properties: The ABINIT software project, Comput. Mater. Sci. **25**, 478 (2002).

[29] G. Kresse and J. Furthmüller, Efficiency of ab-initio total energy calculations for metals and semiconductors using a plane-wave basis set, Comput. Mater. Sci. **6**, 15 (1996).

[30] M. Kurita, K. Nakagawa, and F. Akao, Photoacoustic spectrum in superionic conductors Ag_3SI and AgI, Jpn. J. Appl. Phys. **27**, L1920 (1988).

[31] S. Maintz, V. L. Deringer, A. L. Tchougreeff, and R. Dronskowski, Analytic projection from plane-wave and PAW wavefunctions and application to chemical-bonding analysis in solids, J. Comput. Chem. **34**, 2557 (2013).

[32] J. Heyd, G. E. Scuseria, and M. Ernzerhof, Hybrid functionals based on a screened Coulomb potential, J. Chem. Phys. **118**, 8207 (2003).

[33] L. Schimka, J. Harl, and G. Kresse, Improved hybrid functional for solids: The HSEsol functional, J. Chem. Phys. **134**, 024116 (2011).

[34] G. Pizzi, V. Vitale, R. Arita, S. Blugel, F. Freimuth, G. Geranton, M. Gibertini, D. Gresch, C. Johnson, T. Koretsune *et al.*, Wannier90 as a community code: New features and applications, J. Phys.: Condens. Matter **32**, 165902 (2020).

[35] R. D. King-Smith and D. Vanderbilt, Theory of polarization of crystalline solids, Phys. Rev. B **47**, 1651 (1993).

[36] P. E. Blöchl, Projector augmented-wave method, Phys. Rev. B **50**, 17953 (1994).

[37] G. Kresse and J. Furthmuller, Efficient iterative schemes for *ab initio* total-energy calculations using a plane-wave basis set, Phys. Rev. B **54**, 11169 (1996).

[38] I. Souza, N. Marzari, and D. Vanderbilt, Maximally localized Wannier functions for entangled energy bands, Phys. Rev. B **65**, 035109 (2001).

[39] J. W. Negele, Structure of finite nuclei in the local-density approximation, Phys. Rev. C **1**, 1260 (1970).

[40] J. P. Perdew, A. Ruzsinszky, G. I. Csonka, O. A. Vydrov, G. E. Scuseria, L. A. Constantin, X. Zhou, and K. Burke, Restoring the density-gradient expansion for exchange in solids and surfaces, Phys. Rev. Lett. **100**, 136406 (2008).

[41] J. P. Perdew, K. Burke, and M. Ernzerhof, Generalized gradient approximation made simple, Phys. Rev. Lett. **77**, 3865 (1996).

[42] K. Fischer, H. Bilz, R. Haberkorn, and W. Weber, Covalency and deformability of Ag^+-ions in the lattice dynamics of silver halides, Phys. Status Solidi B **54**, 285 (1972).

[43] A. Togo and I. Tanaka, First principles phonon calculations in materials science, Scr. Mater. **108**, 1 (2015).

[44] M. I. Aroyo, J. M. Perez-Mato, C. Capillas, E. Kroumova, S. Ivantchev, G. Madariaga, A. Kirov, and H. Wondratschek, Bilbao Crystallographic Server: I. Databases and crystallographic computing programs, Z. Kristallogr. **221**, 15 (2006).

[45] S. Hull, D. A. Keen, N. J. G. Gardner, and W. Hayes, The crystal structures of superionic Ag_3SI, J. Phys.: Condens. Matter **13**, 2295 (2001).

[46] A. Kojima and F. Akao, Anomalies of acoustic attenuation and velocity at the β-γ phase transition in Ag_3SI, J. Phys. Soc. Jpn. **51**, 2377 (1982).

[47] A. K. Jahja, Y. Ishii Marsongkohadi, Y. Morii, and Y. Hamaguchi, Diffuse neutron scattering from ordered phase of Ag_3SI at 128K, J. Phys. Chem. Solids **60**, 273 (1999).

[48] P. C. Müller, C. Ertural, J. Hempelmann, and R. Dronskowski, Crystal orbital bond index: Covalent bond orders in solids, J. Phys. Chem. C **125**, 7959 (2021).

[49] R. Dronskowski and P. E. Bloechl, Crystal orbital Hamilton populations (COHP): Energy-resolved visualization of chemical bonding in solids based on density-functional calculations, J. Phys. Chem. C **97**, 8617 (2002).

[50] N. Marzari and D. Vanderbilt, Maximally localized generalized Wannier functions for composite energy bands, Phys. Rev. B **56**, 12847 (1997).

[51] M. Kobayashi, S. Ono, and T. Tomoyose, Electronic structure and covalency in superionic conductors, Ionics **10**, 415 (2004).

[52] T. Kohda, S. Ono, M. Kobayashi, H. Iyetomi, and S. Kashida, *p-d* hybridization and superionicity in silver ternary compounds, J. Phys. Soc. Jpn. **70**, 2689 (2001).

[53] S. Ono, M. Kobayashi, H. Iyetomi, and T. Tomoyose, Difference of *p-d* hybridization in noble metal halides, Solid State Ionics **139**, 249 (2001).

[54] M. Kobayashi, S. Ono, T. Kohda, H. Iyetomi, S. Kashida, and T. Tomoyose, *p-d* hybridization in superionic conductors, Solid State Ionics **154**, 209 (2002).

[55] D. R. Hamann and D. Vanderbilt, Maximally localized Wannier functions for GW quasiparticles, Phys. Rev. B **79**, 045109 (2009).

[56] A. Walsh, D. J. Payne, R. G. Egdell, and G. W. Watson, Stereochemistry of post-transition metal oxides: Revision of the classical lone pair model, Chem. Soc. Rev. **40**, 4455 (2011).

[57] A. Walsh and G. W. Watson, Influence of the anion on lone pair formation in Sn(II) monochalcogenides: A DFT study, J. Phys. Chem. B **109**, 18868 (2005).

[58] J. M. Zuo, M. Kim, M. O'Keeffe, and J. C. H. Spence, Direct observation of *d*-orbital holes and Cu-Cu bonding in Cu_2O, Nature (London) **401**, 49 (1999).

[59] H. X. Deng, J. W. Luo, S. S. Li, and S. H. Wei, Origin of the distinct diffusion behaviors of Cu and Ag in covalent and ionic semiconductors, Phys. Rev. Lett. **117**, 165901 (2016).

[60] E. Gaudin, F. Boucher, and M. Evain, Some factors governing Ag^+ and Cu^+ low coordination in chalcogenide environments, J. Solid State Chem. **160**, 212 (2001).

[61] P. Marksteiner, P. Blaha, and K. Schwarz, Electronic structure and binding mechanism of Cu_2O, Z. Phys. B **64**, 119 (1986).

[62] S. H. Wei, S. B. Zhang, and A. Zunger, Off-center atomic displacements in zinc-blende semiconductor, Phys. Rev. Lett. **70**, 1639 (1993).

[63] C. H. Perry and D. B. Hall, Temperature dependence of the Raman spectrum of $BaTiO_3$, Phys. Rev. Lett. **15**, 700 (1965).

[64] R. A. Evarestov and A. V. Bandura, First-principles calculations on the four phases of $BaTiO_3$, J. Comput. Chem. **33**, 1123 (2012).

[65] G. Henkelman, B. P. Uberuaga, and H. Jónsson, A climbing image nudged elastic band method for finding saddle points and minimum energy paths, J. Chem. Phys. **113**, 9901 (2000).

[66] O. Diéguez and D. Vanderbilt, Theoretical study of ferroelectric potassium nitrate, Phys. Rev. B **76**, 134101 (2007).

[67] S. M. Neumayer, N. Bauer, S. Basun, B. S. Conner, M. A. Susner, M. O. Lavrentovich, and P. Maksymovych, Dynamic stabilization of metastable states in triple-well ferroelectric $Sn_2P_2S_6$, Adv. Mater. **35**, 2211194 (2023).

[68] M. Hoffmann, F. P. G. Fengler, M. Herzig, T. Mittmann, B. Max, U. Schroeder, R. Negrea, P. Lucian, S. Slesazeck, and T. Mikolajick, Unveiling the double-well energy landscape in a ferroelectric layer, Nature (London) **565**, 464 (2019).

[69] K. K. Kobayashi, Dynamical theory of the phase transition in KH_2PO_4-type ferroelectric crystals, J. Phys. Soc. Jpn. **24**, 497 (1968).

[70] T. Tybell, P. Paruch, T. Giamarchi, and J. M. Triscone, Domain wall creep in epitaxial ferroelectric $Pb(Zr_{0.2}Ti_{0.08})O_3$ thin films, Phys. Rev. Lett. **89**, 097601 (2002).

[71] E. Bousquet and P. Ghosez, First-principles study of barium titanate under hydrostatic pressure, Phys. Rev. B **74**, 180101(R) (2006).

[72] I. A. Kornev and L. Bellaiche, The nature of ferroelectricity under pressure, Phase Transit. **80**, 385 (2007).

[73] W. Zhong, R. D. King-Smith, and D. Vanderbilt, Giant LO-TO splittings in perovskite ferroelectrics, Phys. Rev. Lett. **72**, 3618 (1994).

[74] W. Zhong, D. Vanderbilt, and K. M. Rabe, First-principles theory of ferroelectric phase transitions for perovskites: The case of $BaTiO_3$, Phys. Rev. B **52**, 6301 (1995).

[75] M. Markov, L. Alaerts, H. P. C. Miranda, G. Petretto, W. Chen, J. George, E. Bousquet, P. Ghosez, G. M. Rignanese, and G. Hautier, Ferroelectricity and multiferroicity in anti-Ruddlesden-Popper structures, Proc. Natl. Acad. Sci. USA **118**, e2026020118 (2021).

[76] P. Li, X. Ren, G. C. Guo, and L. He, The origin of hyperferroelectricity in $LiBO_3$ (B = V, Nb, Ta, Os), Sci. Rep. **6**, 34085 (2016).

[77] M. Khedidji, D. Amoroso, and H. Djani, Microscopic mechanisms behind hyperferroelectricity, Phys. Rev. B **103**, 014116 (2021).

[78] H. J. Xiang, Origin of polar distortion in $LiNbO_3$-type "ferroelectric" metals: Role of *A*-site instability and short-range interactions, Phys. Rev. B **90**, 094108 (2014).

[79] S. Baroni, S. De Gironcoli, A. Dal Corso, and P. Giannozzi, Phonons and related crystal properties from density-functional perturbation theory, Rev. Mod. Phys. **73**, 515 (2001).

[80] J. F. Nye, *Physical Properties of Crystals: Their Representation by Tensors and Matrices* (Oxford University Press, Oxford, 1985).

[81] S. Roberts, Dielectric and piezoelectric properties of barium titanate, Phys. Rev. **71**, 890 (1947).

[82] S. Liu and R. E. Cohen, Origin of negative longitudinal piezoelectric effect, Phys. Rev. Lett. **119**, 207601 (2017).

[83] A. Dal Corso, M. Posternak, R. Resta, and A. Baldereschi, *Ab initio* study of piezoelectricity and spontaneous polarization in ZnO, Phys. Rev. B **50**, 10715 (1994).

[84] L. Bellaiche and D. Vanderbilt, Virtual crystal approximation revisited: Application to dielectric and piezoelectric properties of perovskites, Phys. Rev. B **61**, 7877 (2000).

[85] X. Wu, D. Vanderbilt, and D. R. Hamann, Systematic treatment of displacements, strains, and electric fields in density-functional perturbation theory, Phys. Rev. B **72**, 035105 (2005).

[86] Y. Qi and A. M. Rappe, Widespread negative longitudinal piezoelectric responses in ferroelectric crystals with layered structures, Phys. Rev. Lett. **126**, 217601 (2021).

[87] N. Ding, H. Ye, and S. Dong, Quasi-one-dimensional sliding ferroelectricity in NbI_4, Phys. Rev. B **110**, 024115 (2024).

[88] N. Ding, J. Chen, C. Gui, H. You, X. Yao, and S. Dong, Phase competition and negative piezoelectricity in interlayer-sliding ferroelectric ZrI_2, Phys. Rev. Mater. **5**, 084405 (2021).

[89] S. Dutta, P. Buragohain, S. Glinsek, C. Richter, H. Aramberri, H. Lu, U. Schroeder, E. Defay, A. Gruverman, and J. Iniguez, Piezoelectricity in hafnia, Nat. Commun. **12**, 7301 (2021).

[90] Y. Hong, J. Deng, Q. Kong, Y. Yin, X. Ding, J. Sun, and J. Z. Liu, Origin of different piezoelectric responses in elemental Sb and Bi monolayers, Phys. Rev. B **109**, 035204 (2024).